Volume 15
Number 33
7 September 2024
Pages 13115–13560

Chemical Science

rsc.li/chemical-science

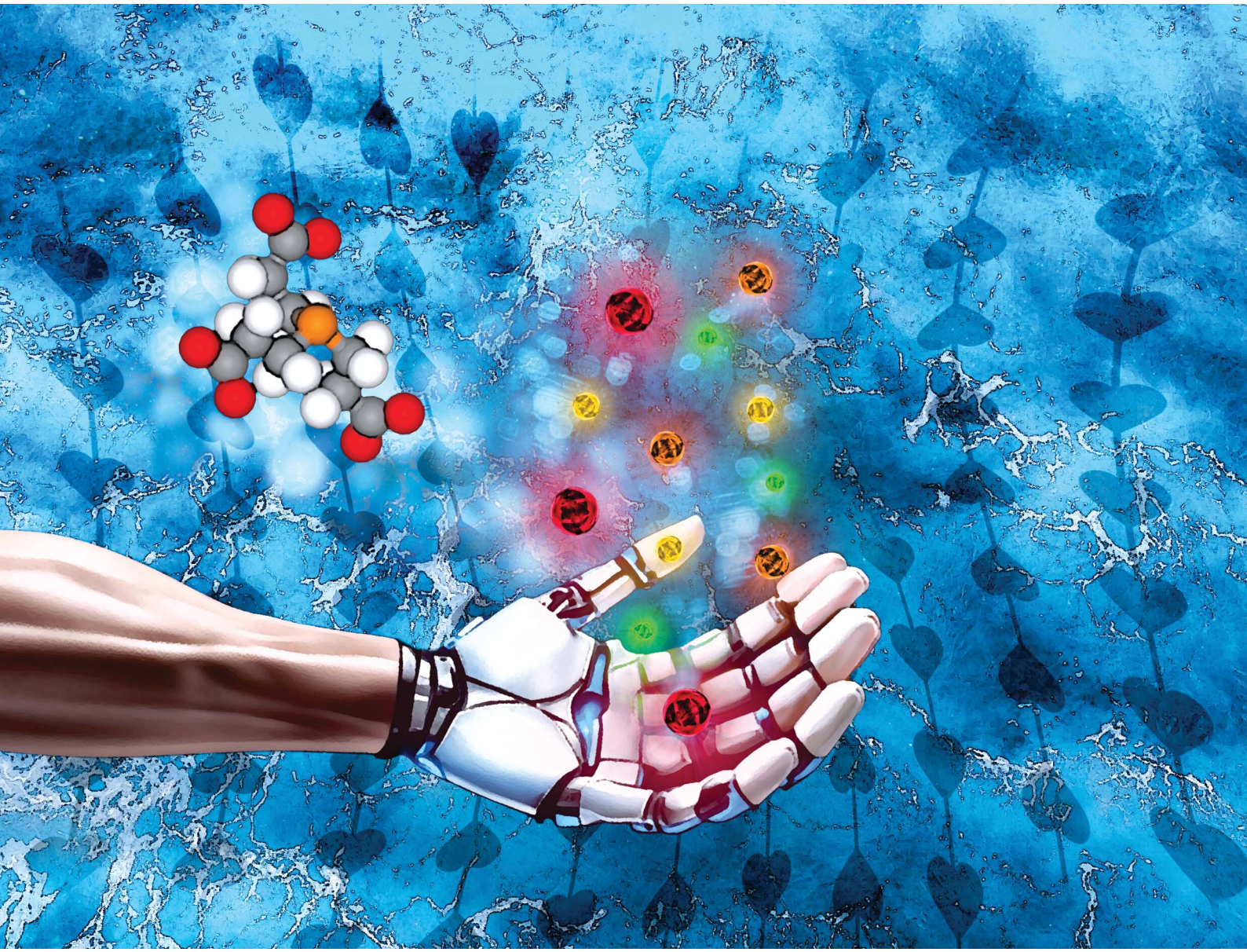

ISSN 2041-6539

ROYAL SOCIETY OF CHEMISTRY

EDGE ARTICLE

Jean-Christophe M. Monbaliu *et al.*

An innovative chalcogenide transfer agent for improved aqueous quantum dot synthesis

Chemical Science

ROYAL SOCIETY OF CHEMISTRY

EDGE ARTICLE

View Article Online
View Journal | View Issue

Cite this: *Chem. Sci.*, 2024, **15**, 13148

All publication charges for this article have been paid for by the Royal Society of Chemistry

Received 17th February 2024
Accepted 26th July 2024

DOI: 10.1039/d4sc01135j

rsc.li/chemical-science

An innovative chalcogenide transfer agent for improved aqueous quantum dot synthesis†

Guillaume Petit,[a] Cedric Malherbe,[b] Pauline Bianchi[a] and Jean-Christophe M. Monbaliu*[ac]

An innovative approach to chalcogenide precursor synthesis and their subsequent use for the production of **CdX** (X = S, Se, Te) quantum dots (QDs) in water under scalable and intensified continuous flow conditions is introduced. Herein, tris(2-carboxyethyl)phosphine (**TCEP**) is identified as a novel, efficient and water-soluble vehicle for chalcogenide transfer to form **CdX** QDs under aqueous conditions. A comprehensive exploration of critical process parameters, including pH, chalcogen excess, and residence time, utilizing a Design of Experiments (DoE) approach is reported. Reaction kinetics are investigated in real-time using a combination of *in situ* Raman spectroscopy and in-line ^{31}P NMR spectroscopy. The conversion of **TCEP** into **TCEP**=X (X = S, Se, Te) species is seamlessly adapted to continuous flow conditions. **TCEP**=X precursors are subsequently employed in the synthesis of **CdX** QDs. Scalability trials are successfully demonstrated, with experiments conducted at flow rates of up to 80 mL min^{-1} using a commercially available mesofluidic flow reactor with favorable metrics. Furthermore, biocompatible and aqueous **CdSe/ZnS** core–shell QDs are for the first time prepared in flow within a fully concatenated process. These results emphasize the potential for widespread biological or industrial applications of this novel protocol.

Introduction

Since their discovery in the early 1980s, Quantum Dots (QDs) have attracted substantial attention from the scientific community. The recent Nobel Prize in Chemistry, awarded to Bawendi, Brus and Ekimov for their groundbreaking work related to QDs, clearly emphasizes their profound impact on the field.[1–4] This interest is mainly due to their tunable optoelectronic properties. The band gap of these nanoscale semiconductors can be finely tuned by altering their size, a consequence of the quantum confinement effect on the electron–hole pairs generated within the particle. This confinement leads to an increase in the energy gap as the particle size decreases.[3,5] This remarkable tunability renders QDs highly attractive for a wide range of applications, including photovoltaic devices,[6,7] LEDs (QLEDs),[8,9] photodetection,[10,11] photocatalysts[12,13] and in bioimaging.[14,15]

Since the early 2000s, the emergence of new process technologies has set new grounds for the development of customizable and scalable methods for producing high-quality QDs. Continuous micro- and mesofluidic processes have already shown significant promise in this regard.[16] It is now well-established among the Chemistry and Chemical Engineering communities that flow processes offer precise control over various reaction parameters, including heat transfer, mixing efficiency and residence time.[17,18] All these reaction parameters are critical for the successful preparation of QDs.[19–22]

Among nanosized semiconductors, type II-VI QDs, and more specifically cadmium chalcogenides QDs (*i.e.*, **CdX** where X = S, Se, Te) have been extensively studied.[23] The hot-injection synthesis is the easiest method to translate under flow conditions for their preparation. This fast-heating process can be performed both in an organic or in an aqueous solvent. Most of these protocols involve the use of a soluble chalcogen transfer agent as well as stabilizing agents. Various types of chalcogen sources have been studied such as trioctylphosphochalcogenides,[4,21,24–28] tributylphospho-chalcogenides[20,29] and those chelated by the solvent itself (such as octadecene[24]). Some representative synthetic protocols under flow conditions for the preparation of QDs are illustrated in Fig. 1.

While generating QDs in an organic medium is notoriously easier to control, the use of a polar, lipophilic stabilizing agents limits their compatibility with downstream applications. This often requires additional steps, such as ligand exchange to enable compatibility with polar solvents.[30,31] On the contrary,

[a]*Center for Integrated Technology and Organic Synthesis (CiTOS), MolSys Research Unit, University of Liège, B-4000 Liège (Sart Tilman), Belgium. E-mail: jc.monbaliu@uliege.be; Web: https://www.citos.uliege.be/*

[b]*Mass Spectrometry Laboratory, MolSys Research Unit, University of Liège, B-4000 Liège (Sart Tilman), Belgium*

[c]*WEL Research Institute, Avenue Pasteur 6, B-1300 Wavre, Belgium*

† Electronic supplementary information (ESI) available: Detailed experimental protocols, microfluidic and mesofluidic setups. See DOI: https://doi.org/10.1039/d4sc01135j

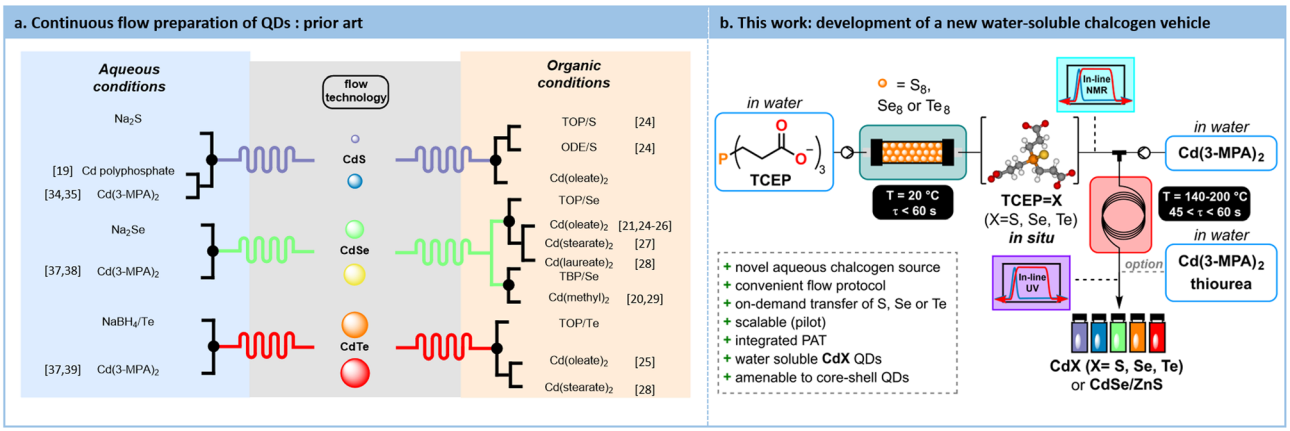

Fig. 1 (a) Protocols from the prior Art for accessing QDs with flow processes. For each chalcogen (S, Se, Te), the precursors are summarized according to the reaction medium (organic/aqueous). (b) This work reports a fully concatenated flow process in water for accessing **CdX** (X = S, Se, Te) QDs, as well as **CdSe/ZnS** core–shell QDs.

aqueous synthesis offers several advantages such as offering biocompatibility, requiring no additional ligand exchange steps, and operating at lower temperatures, compared to organic phase syntheses. However, aqueous protocols often lead to broader size distribution and lower quantum yield.[32,33] Moreover, the relatively limited number of reports using aqueous protocols suggests that they are more cumbersome compared to their organic counterparts.

One of the challenges in synthesizing QDs in water lies in the preparation of a suitable reduced chalcogen source, which is essential for initiating the transfer to the cadmium precursor and producing QDs. All reported protocols involve an *ex situ* preparation of the chalcogenide precursor in batch, which could potentially lead to its decomposition. These protocols typically rely on the reduction of native chalcogens with ionic reductants such as $NaBH_4$ to give air-sensitive ionic chalcogenides such as Na_2S,[19,34,35] Na_2Se[36–38] or NaHTe.[37,39] Their decomposition prevents a seamless scale-up that continuous flow argues to offer. Moreover, reports dealing with the aqueous preparation of QDs in flow often do not report their photoluminescence quantum yield (PLQY).[40]

Capitalizing on these unmet needs for the scalable aqueous preparation of QDs and on our expertise in flow chemistry,[41–46] a concrete solution for developing a robust and innovative water-soluble chalcogenide source is sought. Tris(2-carboxyethyl)phosphine (**TCEP**) emerged as a highly effective water-soluble vehicle for reduced chalcogens to yield **CdX** (X = S, Se, Te) QDs. The impact of various parameters such as pH, chalcogen excess, and residence time on the conversion toward **TCEP**=X is explored through a Design of Experiments (DoE) approach. The reduction kinetics and the formation of **TCEP**=X species are studied *via in situ* Raman spectroscopy. This reaction is then successfully adapted to continuous flow conditions with in-line low-field ^{31}P NMR monitoring. Subsequently, these novel water-soluble chalcogenide precursors are assessed for the synthesis of **CdX** QDs. Furthermore, the long-term process stability and scalability are demonstrated, with trials conducted at flow rates up to 80 mL min^{-1} using a commercial mesofluidic flow reactor. The results demonstrate that this intensified continuous flow aqueous process provides stable **CdX** QDs with short reaction times and high productivity. Additionally, *in situ* generation of chalcogenide precursors in flow prevents their degradation. Biocompatible **CdSe**/**ZnS** core–shell QDs are also produced within 7.25 min in a fully concatenated process. These efforts yield unprecedented process metrics for aqueous QD synthesis.

Results and discussion

Optimization of the preparation of TCEP=X

Since its initial description by Whitesides[47] in 1991, **TCEP** has found widespread synthetic utilities for reducing disulfide bonds in biochemistry, peptide chemistry and desulfurization/deselenization reactions.[48–55] Subsequently, **TCEP**'s utility was broadened to the reduction of various organic functional groups[56,57] and for the coordination of metal cations.[58] The use of **TCEP** in QDs synthesis, however, remains undocumented, either as chalcogen reducing agent or stabilizing phosphine. The initial phase of the project therefore aimed to demonstrate the adaptability of **TCEP** for reducing under aqueous conditions three key chalcogens (sulfur, selenium and tellurium) for the preparation of **CdX** QDs.

Preliminary experiments highlighted a stronger resistance toward air oxidation compared to common sodium-based chalcogenide precursors (Section S4.4.1 in the ESI†). Early trials also emphasized a substantial effect of the pH on the outcomes. Indeed, **TCEP** is a phosphine compound bearing up to 4 exchangeable protons: 3 on the carboxylic acid moieties (pK_a = 2.99, 3.67, 4.36)[59] and 1 on the phosphorus center itself (pK_a = 7.66)[59] (Fig. 2a). The latter proton plays the most influential role in modulating **TCEP**'s reactivity.[58,59]

The substantial impact of pH on **TCEP**'s inherent features becomes evident when comparing the ^{31}P NMR chemical shifts (Fig. 2b, blue spectra) of **TCEP** under acidic conditions (pH value from 5 to 7, δ = 17.5 ppm) and alkaline conditions (pH value from 8 to 11, δ = −20.6 ppm). **TCEP**'s protonation state

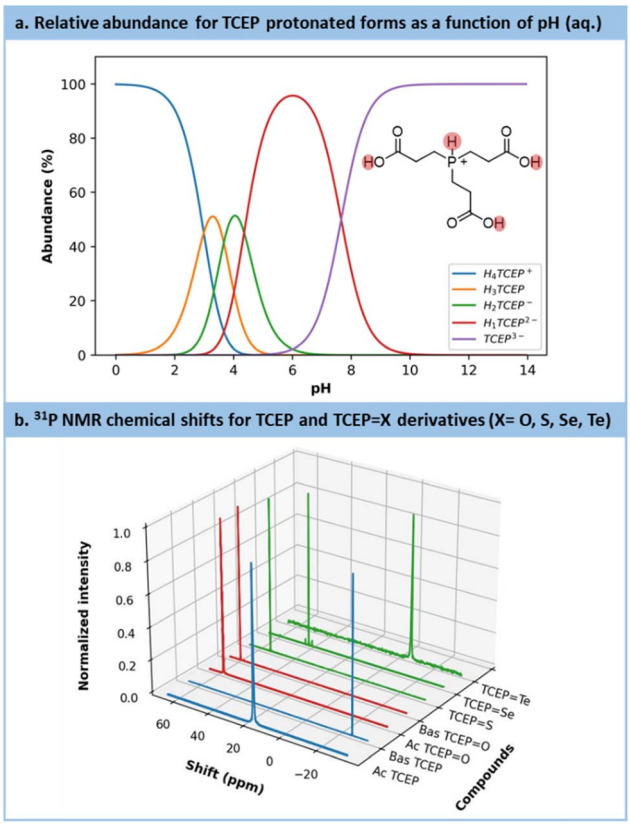

Fig. 2 (a) Calculation of the protonation distribution of TCEP species based on the p*Ka*.[45] (b) Chemical shifts for each TCEP derivates: blue = reagents (TCEP acid (Ac) and basic (Bas) forms), red = side product (TCEP=O acid (Ac) and basic (Bas) forms) and green = the products of interest (TCEP=S, TCEP=Se, TCEP=Te).

particularly exerts a profound influence on the reduction of Te. For the latter, the acidic form of **TCEP** is unable to act as a reductant. Fig. 2b also presents the ^{31}P NMR spectra for **TCEP**=O (δ = 56.9 ppm at pH = 2.5 and 58.9 ppm at pH = 11), **TCEP**=S (δ = 52.7 ppm), **TCEP**=Se (δ = 41.4 ppm) and **TCEP**=Te (δ = −6.8 ppm). The formation of **TCEP**=O as a side product is often observed when solutions of **TCEP**=X are exposed under aerobic conditions, especially at pH > 9. Therefore, to prevent the competing formation of **TCEP**=O, all reactions were carried out under an inert atmosphere.

After identifying pH as the most critical parameter for the preparation of **TCEP**=X, a multifactorial optimization was initiated through a Design of Experiment (DoE), under batch conditions. The reaction between **TCEP** and elemental chalcogens is inherently heterogeneous, hence, apart from pH, 3 additional parameters are likely to influence the reaction: (a) the excess chalcogen, (b) the mixing efficiency and (c) the timeframe for the reaction.

The multifactorial optimization started with the synthesis of **TCEP**=S. A range of preliminary boundary conditions was selected, including pH values of 5 (representing the phosphine in its fully protonated form) and 11 (representing **TCEP** in its deprotonated form); an excess of chalcogen (S_8) ranging from 1.5 to 3 equivalents; stirring speed set between 700 to 900 rpm. Samples were collected after 20, 40 and 60 min. Crude samples were directly analyzed by high-field ^{31}P NMR, after the addition of deuterium oxide (50 : 50 crude/D_2O, in volume).

The preliminary set of results from the DoE was analyzed through an effect plot, which summarizes the relative impact of each parameter on the conversion (Fig. 3a). A model was derived and is summarized as contour plots in Fig. 3c. The effect plot shows that the most conductive parameter to enhance conversion is the excess of chalcogen, contributing to 53.6%, followed by the reaction time to 26.9%. Interestingly, pH exhibits a quadratic effect. Indeed, it was expected that an increasing pH would only have a positive impact; however, this was not the case, since more alkaline conditions triggered a competitive phenomenon, *i.e.*, chalcogen polymerization.[60] Mixing efficiency does not exert a significant direct impact with this range of rpm. However, when expressed as an interaction parameter, it shows a positive influence in conjunction with the reaction time. Moreover, pH and excess of S_8 are also associated with a positive interaction. The model resulting from these results (Fig. 3c) for sulfur reduction with **TCEP** toward **TCEP**=S anticipates full conversion with the simultaneous requirement for extended reaction times (>40 min), a large excess of sulfur (>2.5 eq.) at pH values between 7.5 and 9 (graphical determination), all under vigorous stirring.

Similar behavior can be drawn for the reduction of selenium with **TCEP** toward **TCEP**=Se, emphasizing a significant positive effect of the excess of Se_8, and a milder positive influence of the reaction time. For the preparation of **TCEP**=Se, the pH parameter exhibits a square term with an optimum between 8 and 9.5 (graphical determination). There are also two negative interaction parameters involving the excess Se_8 *vs.* pH or reaction time (*i.e.*, pH·Eq. and Eq.·*t*, Fig. 3b). The model constructed for **TCEP**=Se predicts complete conversion within a shorter reaction time (10 min) and with a lower excess of selenium (up to 1.5 equiv.) (Fig. 3d).

However, in the case of **TCEP**=Te, the optimization strategy needed adaptation. Firstly, as the protonated form of **TCEP** appeared incapable of reducing tellurium, **TCEP** in aqueous solution must be at a pH above 10 to react with Te(0). Secondly, due to the notably faster reduction rate for Te(0), the reaction with **TCEP** occurred within such a short timeframe that ^{31}P NMR reaction monitoring was not doable. Instead, we selected *in situ* Raman spectroscopy (see Fig. 4a and b). This allowed for the assessment of various parameters and their influence on the initial reaction rate (v_i), including the excess of tellurium, its granulometry and mixing efficiency. Note that these preliminary observations were made by using 200 mesh tellurium. After several trials, −18 + 60 mesh tellurium was preferred for easier monitoring.

As illustrated in Fig. 4c, the mixing had only a minor effect on the reaction kinetics, with a mere 2.8% increase while transitioning from 500 to 750 rpm, which confirms the observation made on the effect diagram for **TCEP**=S formation. The excess of Te_8 had a positive effect on the reaction rate constant, accelerating it from 3.56 10^{-4} mol L^{-1} s^{-1} to 7.90 10^{-4} mol L^{-1} s^{-1} when the tellurium excess was increased (1.5 to 3 equiv.). In addition, the granulometry of tellurium had a profound impact

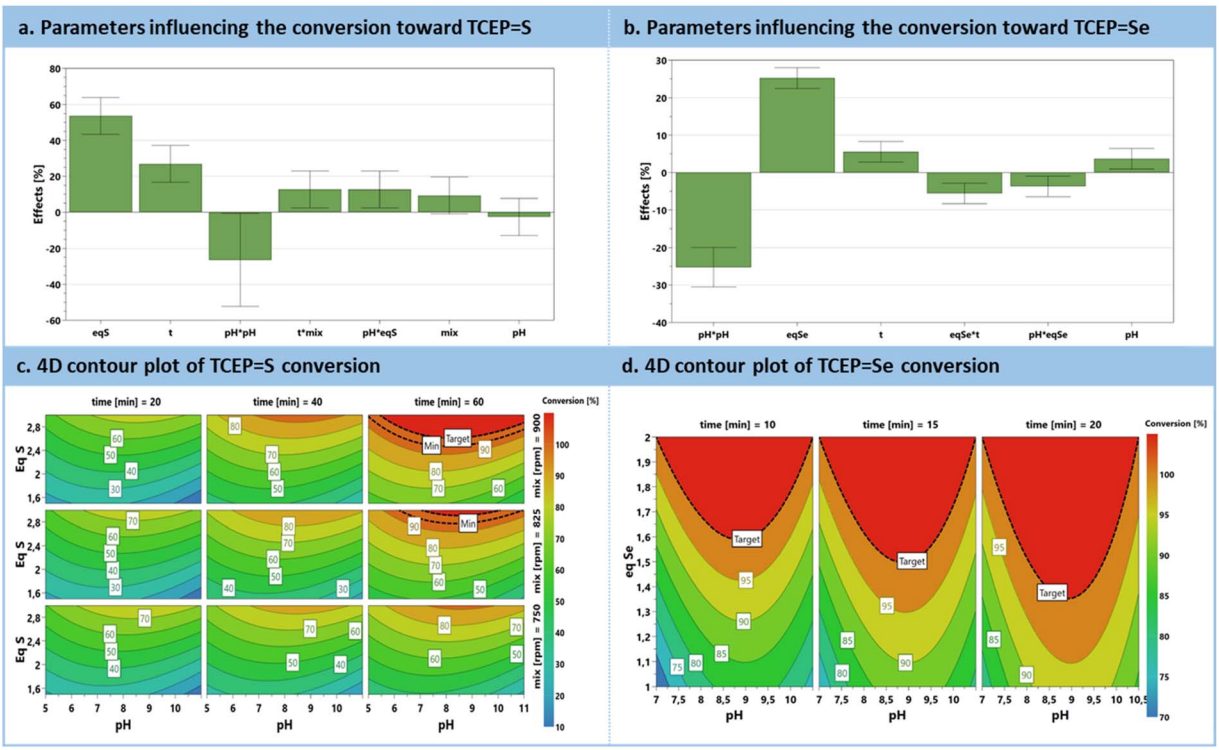

Fig. 3 DoE for the preparation of TCEP═S, Se. (a) Plot of significant parameters influencing the formation of TCEP═S. (b) Plot of significant parameters influencing the formation of TCEP═Se. (c) Contour plot of the model developed for the conversion into TCEP═S. (d) Contour plot of the model developed for the conversion into TCEP═Se.

on the reaction. When switching from −18 + 60 mesh to 200 mesh, *i.e.*, reducing the size of particles from 454 μm (equivalent diameter on volume) to 44 μm, the reaction proceeded 22.41 times faster (from 3.56 10^{-4} mol L^{-1} s^{-1} with particle sizes of 454 μm to 7.96 10^{-3} mol L^{-1} s^{-1} with particle sizes of 44 μm), as shown in Fig. 4d.

To sum up the preliminary batch optimization, pH emerges as a critical factor for reaction rate, especially in the preparation of **TCEP**═Te. For sulfur and selenium, which exhibit a quadratic behavior, synthesis at the optimum pH, *i.e.* moderately basic, is also recommended. The quadratic behavior of the **TCEP**═S, Se formation is likely to be influenced by, at lower pH, the protonation rate of the **TCEP** and, at high pH, the formation of polymeric species.[60] Mixing effects are limited, and at speeds higher than 500 rpm, their influence becomes negligible. An excess of chalcogen has a positive impact on the preparation of all 3 compounds (**TCEP**═S, Se, Te). The effect of the granulometry, which was studied only for the preparation of **TCEP**═Te, clearly shows that smaller particles lead to a drastic increase in kinetics, related to an increase in the surface area of the chalcogen. This is expected in a heterogeneous process where the rate-determining step involves homogeneous reagents (**TCEP**) and the chalcogen surface.

In situ kinetics of the chalcogen reduction by TCEP

Following preliminary optimization and multivariate analysis, a more refined kinetic study was conducted for the reduction of all chalcogens with **TCEP**. Prior to these experiments, precise research on the optimum pH was sought (Fig. S14 in the ESI†). These experiments aimed to determine the reaction mechanism, specific kinetic constants and experimental activation barriers for the rate-determining step. Each substrate (**TCEP**═S, Se, Te) was subjected to the reaction at 30 °C, 40 °C and 50 °C, as well as 60 °C for Se and Te.

The reactions were monitored by *in situ* Raman spectroscopy following a protocol similar to Fig. 4, with the evolution over time of the Raman signal corresponding to the P═X (X = S, Se, Te) bond (P═Te: 376 cm^{-1}; P═Se: 428 cm^{-1}; P═S: 578 cm^{-1}). The results are plotted in Fig. 5a. For each series, the temperature had a positive effect on the reaction kinetics. Similar trends were observed for the reduction of selenium and tellurium with **TCEP**: the reaction initiated rapidly and then slowed down after reaching a concentration of 0.15 mol L^{-1}. The reaction with S_8 followed a different pattern (Fig. S15 and 16 in the ESI†). Initially, a complex and broad signal with characteristic peaks at 500 cm^{-1} and 825–870 cm^{-1} appeared, hypothesized to be adsorbed **TCEP** on the surface of sulfur particles. This transient species eventually leads to the formation of the expected product (**TCEP**═S).

The kinetic data were then used to establish the rate laws governing the preparation of **TCEP**═S, Se, Te. Various models were envisaged, accounting for the critical role of the **TCEP** adsorption of the chalcogen's surface (more details are provided in Section S5.6 of the ESI†). Despite their complexity, none of these models successfully fitted the kinetics data. Nonetheless,

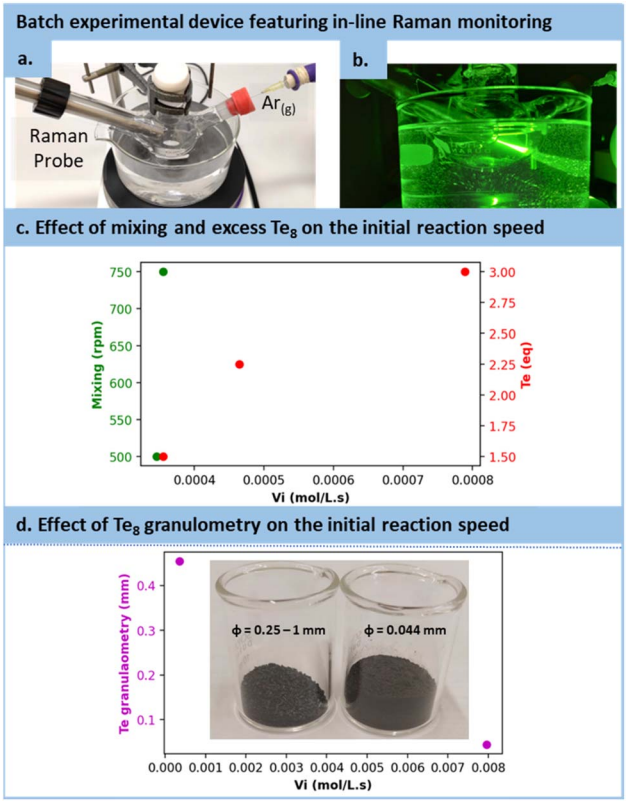

Fig. 4 (a) and (b) Experimental setup with a modified three-necked round-bottom flask allowing to insert an in-line Raman probe and flushing the flask with argon. (c) Influence of the mixing and tellurium excess on the initial reaction speed. (d) Impact of the tellurium granulometry on the initial speed.

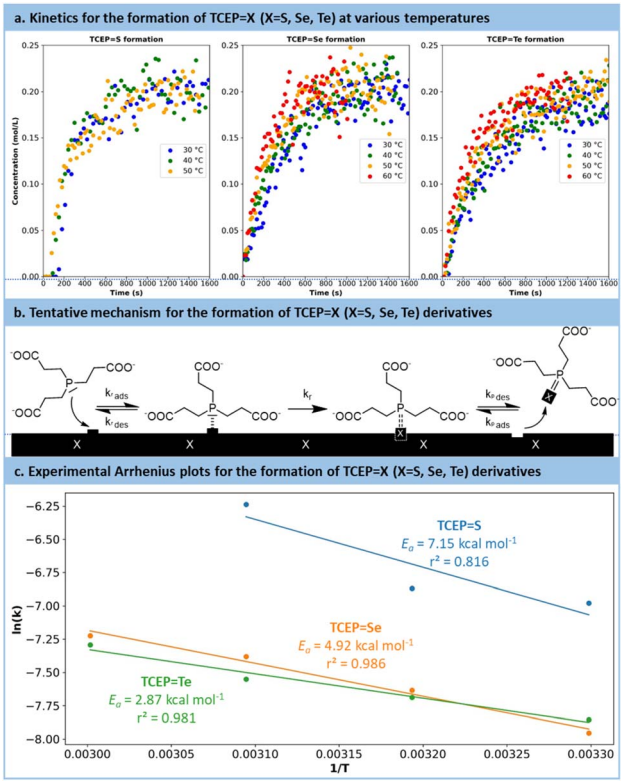

Fig. 5 (a) Crude data obtained during the kinetic monitoring, for each TCEP=X (X = S, Se, Te) derivative. (b) Hypothesized heterogeneous mechanism showing the interaction of TCEP on the surface of the elemental chalcogen. (c) Experimental constant rates and Arrhenius fit for each TCEP=X derivative.

closer examination of the data indicated that the reaction slowed down more rapidly than predicted by the models. A plausible hypothesis to account for this deviation is a decrease in active site accessibility on the chalcogen's surface due to an increase in its porosity (Fig. 5b). This effect was integrated into the model as a decreasing exponential function (Section S5.6 of the ESI†).

The revised kinetic model (eqn (1)) was effectively used to fit the experimental data using eqn (2). With this approach, the kinetic constants were derived for the preparation of **TCEP**=S, Se, Te at 30 °C, 40 °C, 50 °C and 60 °C (the latter temperature was only considered for **TCEP**=Se, Te). These constants were next used to calculate the experimental activation energies for the rate-determining step of the 3 processes using Arrhenius' equation (Fig. 5c and eqn (3)). The values obtained for each species exhibited a periodic trend: **TCEP**=S (7.2 kcal mol^{-1}) > **TCEP**=Se (4.9 kcal mol^{-1}) > **TCEP**=Te (2.9 kcal mol^{-1}). These observations align well with the ones collected during the batch optimization (full conversion was achieved faster with **TCEP**=Te > **TCEP**=Se > **TCEP**=S) and are consistent with existing literature data as well, and follow HSAB theory.[61]

$$r = k_r \cdot \frac{k_a \cdot C(t)}{1 + k_a \cdot C(t)} + C(t) \cdot e^{-k_{dea} \cdot C(t)} \quad (1)$$

$$\frac{C(t)}{r} = \frac{1}{k_r \cdot k_a} + \frac{1}{k_a} \cdot C(t) + e^{k_{dea} \cdot C(t)} \quad (2)$$

$$\ln k_r = \ln A + \frac{E_a}{R} \cdot \frac{1}{T} \quad (3)$$

Eqn (1) shows the chemical rate, where k_r is the constant rate, k_a is the affinity constant for the chalcogen surface and k_{dea} is the deactivation constant of the chalcogen surface; eqn (2) shows the modified kinetic equation useable in 3 parameters fitting; eqn (3) shows the Arrhenius fit to determine the experimental activation barrier, where k_r is the constant rate, A is the pre-exponential factor, E_a is the activation barrier and R is the universal gas constant.

Transposition in flow for the preparation of TCEP=X

Considering the compelling evidence that the reaction, proceeding *via* the adsorption of **TCEP** on the chalcogen particle's surface, is dominated by surface accessibility, there are two potential options to enhance reaction kinetics: increasing the excess of chalcogen and/or reducing chalcogen particle size. These attributes can be effectively combined under continuous flow conditions. Therefore, elemental chalcogen powder was considered as a packing material suitable for packed-bed tubular flow reactors. In this setup, a feed solution of **TCEP**

(0.2 M in water, pH = 10.7) is passed through the packed-bed column containing the elemental chalcogenides.

A versatile flow system was constructed, consisting of 3 columns ($\frac{1}{4}$'' stainless steel, 150 mm length) operated in parallel, each filled with either sulfur, selenium, or tellurium, respectively (Fig. 6a and b). These 3 columns were connected upstream to a single feed solution of **TCEP** through an automated selector valve. The valve was remotely controlled to select the appropriate chalcogen source, enabling on-demand preparation, at room temperature, of **TCEP**═S, **TCEP**═Se, and **TCEP**═Te. For each column, the porosity (ε) was estimated to be 0.287 (S_8), 0.098 (Se_8) and 0.434 (Te_8) (note that −18 + 60 mesh tellurium was used), respectively. These different porosities resulted in varying reactor volumes and chalcogen ratios, thereby impacting the reactivity trends calculated with the activation barriers. The downstream section of the flow setup featured a benchtop low-field NMR operated in the ^{31}P NMR mode to assess both productivity and stability (Fig. 6a and b).

For each chalcogen, a feed solution of **TCEP** (pH 10.7) was infused at flow rates ranging from 0.25 mL min^{-1} to 2 mL min^{-1}. Conversion and space-time yield (STY, see Section S5.7 in the ESI† for more details) were calculated to determine the productivity boundaries of the flow system. In the case of sulfur, full conversion to **TCEP**═S was maintained within the range of 0.25 mL min^{-1} to 2 mL min^{-1} (STY: 45.9 g L^{-1} min^{-1} with an estimated residence time of 0.354 min at 2 mL min^{-1}). Similar results were observed for **TCEP**═Te (STY: 61.5 g L^{-1} min^{-1} and an estimated residence time of 0.534 min at 2 mL min^{-1}).

For **TCEP**═Se, full conversion was observed up to 1 mL min^{-1} (STY: 26.8 g L^{-1} min^{-1} and an estimated residence time of 0.242 min), as illustrated in Fig. 6c. These outcomes are particularly remarkable when compared to kinetic batch experiments, where full conversion required approximately 20, 23, and 26 min for sulfur, selenium, and tellurium, respectively. The substantial reduction in the timeframe and the outstanding productivity metrics required to achieve full conversion emphasize the advantages of this flow setup for the reduction of chalcogens.

Continuous monitoring of **TCEP**═Te at a flow rate of 1.2 mL min^{-1} was conducted and sustained full conversion for a total operation time of 200 min, which is quite promising in anticipation of scalability trials for **CdTe** QDs (see below, and Fig. S25 in the ESI†).

Concatenation to the downstream preparation of quantum dots

The direct concatenation of the upstream generator for **TCEP**═X with the downstream preparation of **CdX** significantly reduces the risk of precursor degradation and enhances the versatility of the flow setup (Fig. 7a). The aqueous protocol for

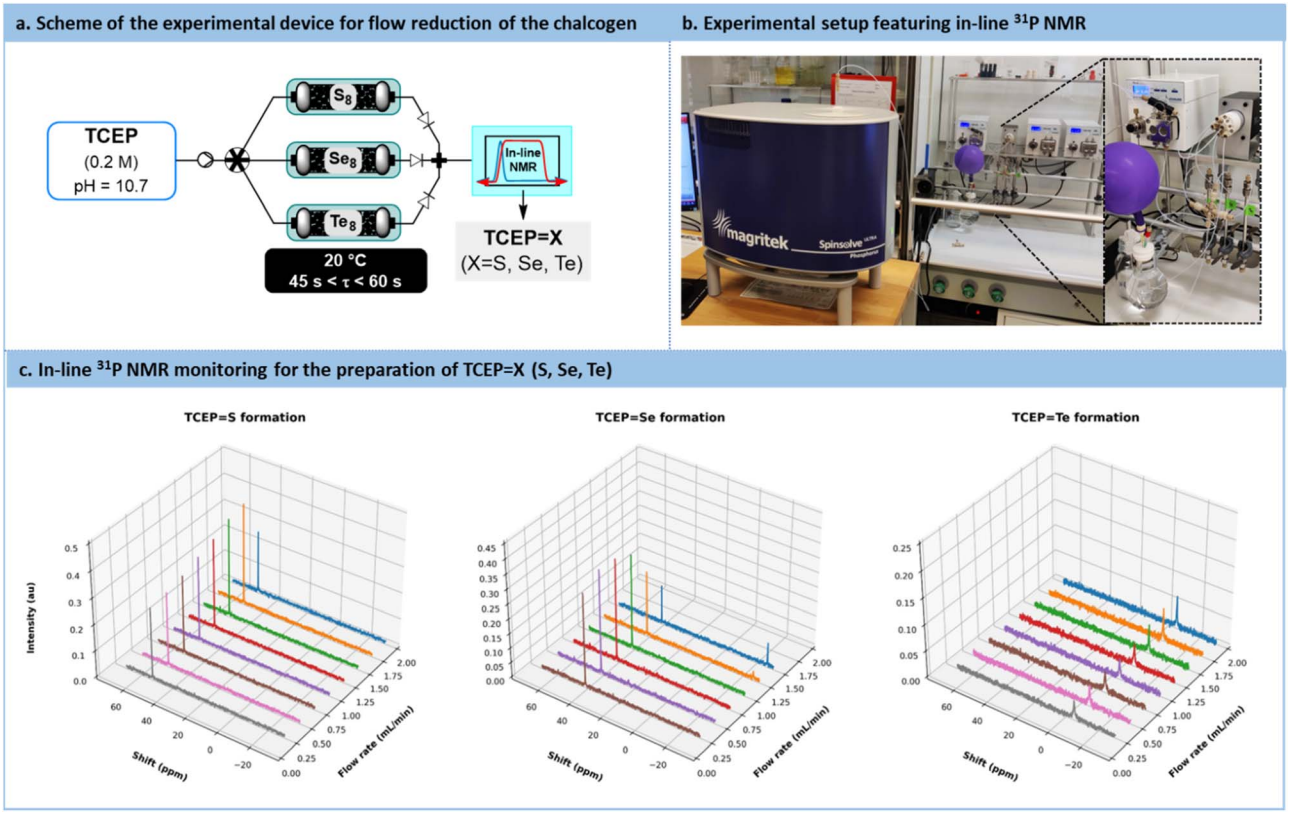

Fig. 6 (a) Simplified flow chart of the automated flow system featuring 3 packed-bed reactors (filled with sulfur, selenium, or tellurium) and operated in parallel. (b) Photograph of the experimental device, emphasizing the in-line low field benchtop ^{31}P NMR. (c) Reaction monitoring (^{31}P NMR) for the production of **TCEP**═X (X = S, Se, Te) species.

CdX synthesis was adapted to accommodate our system, taking advantage of the distinctive features of the new chalcogenide precursor, **TCEP**=X. Typically, these protocols involve a strongly basic solution (pH > 11) and cadmium mercaptopropionate (**Cd(3-MPA)$_2$**) as cadmium precursor.[62]

In the proposed system, the **TCEP**=X generator (Fig. 7a) was inserted upstream of an additional static mixer. The latter allowed the stream of **TCEP**=X to be blended with a feed solution of **Cd(3-MPA)$_2$**. The resulting reaction mixture was then directed to a heated reaction coil for QD generation. The reactor effluent was thermally quenched and then connected to an in-line UV-VIS spectrometer for real-time reaction monitoring.

The results obtained during the synthesis are shown in Fig. 7b. Overall, these results demonstrate the effectiveness of fresh **TCEP**=X precursors as efficient chalcogenide carriers under aqueous conditions. They demonstrate the capability of **TCEP**=X to readily transfer chalcogen to cadmium under relatively mild conditions. Furthermore, the findings highlight that the reactivity of **TCEP**=X is significantly influenced by the nature of the chalcogen, establishing a reactivity hierarchy where softer chalcogens (**TCEP**=S < **TCEP**=Se < **TCEP**=Te) require lower process temperatures.

High-resolution transmission electron microscopy (HRTEM) and powder X-ray diffraction (PXRD) analyses were conducted to provide insights into the size and morphology of the QDs (Fig. 8a). The HRTEM images revealed that the particles exhibited a spherical morphology, with estimated particle sizes of 3.31 nm for **CdS**, 3.35 nm for **CdSe**, and 4.0 nm for **CdTe** (Fig. 8a). Subsequently, PXRD analyses were carried out on purified QDs, utilizing zero-background substrates. For all three samples (**CdX**, where X=S, Se, and Te), the XRD patterns matched those of reference samples, confirming the crystalline nature of the QDs (Fig. 8b). These QDs exhibited a cubic crystal system.

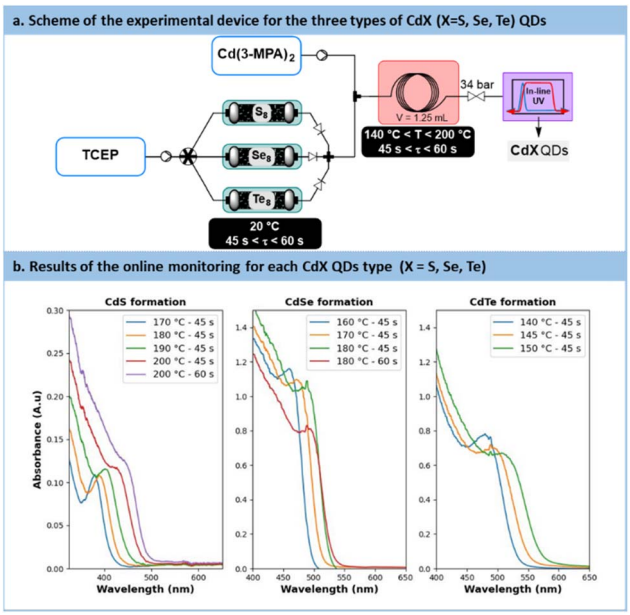

Fig. 7 (a) Simplified flow chart for the concatenated process towards **CdS**, **CdSe** and **CdTe** QDs. (b) In-line monitoring with UV/vis. (A.u. = Absorbance units), path length: **CdS** 0.5 mm, **CdSe/Te**: 10 mm.

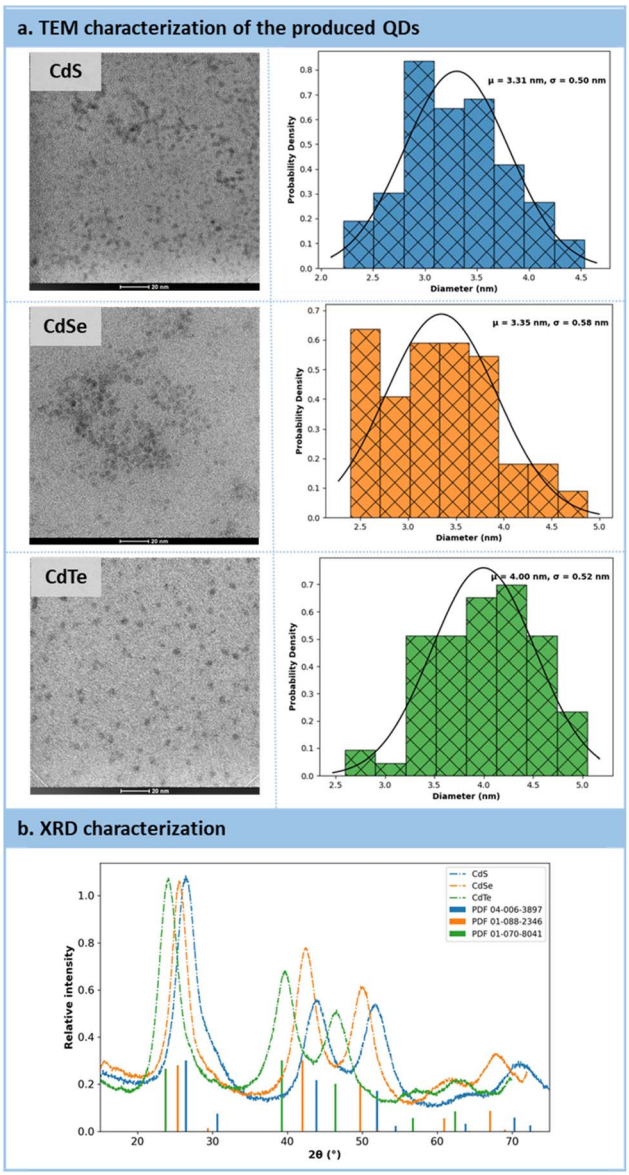

Fig. 8 (a) Characterizations of QDs after their production by HRTEM. (b) Characterizations of QDs by Powder X-ray Diffraction analysis.

The size of QDs, including their ligand corona, can also be determined through diffusion-ordered spectroscopy (DOSY) NMR experiment.[63,64] DOSY correlates ^{1}H NMR chemical shifts with diffusion coefficients, enabling precise attribution of the hydrodynamic diameters of the particles and their surface ligands. Accordingly, the following hydrodynamic diameters were attributed to each QD type: **CdS** 4.67 nm, **CdSe**: 5.67 nm, **CdTe**: 4.70 nm. The chemical shifts corresponding to these hydrodynamic diameters were associated with the methylene groups of 3-MPA (broad signals at approximately 2.93 ppm and 2.56 ppm). Despite thorough purification was carried out before characterization, phosphorus signals from phosphine oxide, a known stabilizing agent, were also detected. The peak width

suggested their presence as "free ligands".[63] This hypothesis was confirmed by X-ray photoelectron spectroscopy (XPS), which did not show any phosphorus 2p interactions (likely lost during the high vacuum before analysis), but revealed unsaturated metal. XPS also highlighted a significant proportion of carboxylate functions, likely from 3-MPA, **TCEP**═O (through the 3 carboxylate functions), and acetate ions from the cadmium source. Surface analysis indicated a cadmium-to-chalcogen ratio of less than 1 (around 0.4), suggesting a surface alloy $\mathbf{CdX}_n\mathbf{S}_{n-1}$ (X = Se, Te) not detectable by XRD. Finally, the presence of a thiolate–cadmium bond was confirmed.

Proof of concept with CdS QDs

In the case of **CdS**, a temperature range of 170 °C to 200 °C, as well as residence times ranging from 45 s to 60 s, were investigated. The UV absorbance monitoring (Fig. 7b) revealed an excitonic peak shifting from 380 nm to 435 nm, thus indicating an increase in particle size with higher temperatures and longer residence time. Moreover, absorbance values increased from 0.11 to 0.13, thus indicating an increase in particle concentration and, consequently, enhanced nucleation efficiency.

However, the presence of a large Stokes shift revealed photoluminescence properties characterized by trap states instead of excitonic emission.[65] This emission similar to colloidal **CdS** has been already reported previously[66] and seems characteristic of some aqueous carboxyl-capped **CdS** QDs. Efforts to suppress these vacancies were unsuccessful, even by working with an excess of Cd^{2+} or opting for core–shell QDs. A deeper investigation is necessary for the **CdS** QDs formed with this method. However, to rule out the possibility of 3-MPA as a potential source for sulfur transfer under aqueous conditions, a control experiment was conducted (see Section S5.9 of the ESI†). The synthesis was repeated without **TCEP**═S, and it did not yield high-quality **CdS** QDs. With all converging proofs toward the development of a new and effective vehicle for chalcogenides under aqueous process conditions, further applications benefiting from flow technology were envisaged.

Type I CdSe/ZnS core–shell QDs

Temperatures ranging from 160 °C to 180 °C and residence times from 45 s to 60 s were explored for the preparation of **CdSe** QDs. With such conditions, a minor decrease in absorbance from 1.18 to 0.8 pointing out a reduction in **CdSe** particle concentration. Conversely, particle size increased, with a peak red-shifted from 475 nm to 500 nm. Similarly to previous reports in the literature, **CdSe** QDs showed poor emission spectra (Fig. S56 in the ESI†). A common strategy to passivate surface trap states is to add a semiconducting shell bearing a higher bandgap.[67,68] **CdSe**/**ZnS** core-shells QDs are frequently investigated for their improved photoluminescence and reduced toxicology profile.[69] Our approach was amenable to a direct concatenation of the module for preparing **CdSe** QDs (Fig. 9a).

Therefore, the reactor effluent containing **CdSe** was mixed with a basic feed of $ZnCl_2$, thiourea as the sulfide donor and

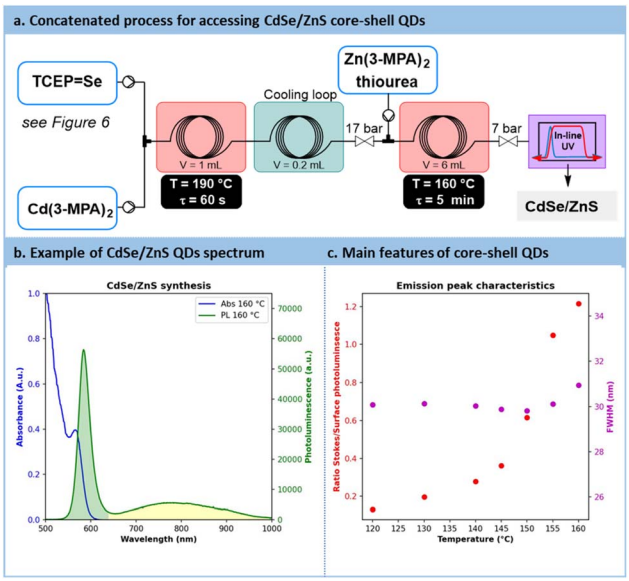

Fig. 9 Passivation of surface trap states through the preparation of **CdSe**/**ZnS** core–shell QDs. (a) Concatenated process with the injection of $Zn(3\text{-MPA})_2$ and thiourea downstream the preparation of **CdSe** QDs. (b). Absorbance (blue line, A.u. = Absorbance units) and photoluminescence (green line, a.u. = arbitrary unit) of **CdSe**/**ZnS** QDs. (c) Effect of the temperature on the ratio fluorescence/surface emission (red scatter) and the peak full width at half maximum (FWHM) (magenta scatter).

3-MPA as the stabilizing agent (see Section S4.8 of the ESI†). The corresponding setup is illustrated in Fig. 9a. Adding **ZnS** at temperatures ranging between 120 °C and 160 °C for 5 min led to core–shell QDs with a strong excitonic peak localized around 585 nm. Trap state emission was drastically reduced. To quantify the improvement in emission, a new metric was introduced: the ratio of the fluorescence peak to the trap state emission, depicted as the green surface over the yellow surface ratio in Fig. 9b (see Section S5.12 of the ESI†). This metric, presented in Fig. 9c, revealed a constant increase of this ratio from 0.13 (120 °C) up to 1.2 (160 °C). These results demonstrate that adding a **ZnS** shell over the **CdSe** core significantly improves the emission properties, even from an initially modest starting point. Additionally, the **ZnS** shell appears to have a limited impact on QD size, as the full width at half maximum (FWHM) remains consistently around 30 nm across different temperatures (Fig. 9c). This new protocol offers a fully concatenated process where each operating parameter can be tuned individually, highlighting the potential of this innovative approach for preparing high-quality biocompatible nanomaterials.[68] To the best of our knowledge, this is the first report on a concatenated flow protocol for the preparation of high-quality aqueous **CdSe**/**ZnS** core–shell QDs and that does not require downstream ligand exchange.[28]

Optimization and reaction insights for CdTe QDs synthesis

The initial trials showed that **CdTe** was the most promising QD core. **CdTe** QDs exhibited limited trap state emission under mild reaction temperatures. Those conditions are usually

compatible with most commercial mesofluidic reactors, thus opening doors for potential scalability.[70] Before carrying out further optimization, data were collected on the inherent mechanistic features for the preparation of **CdTe**. According to the literature focusing on organic phosphine-chalcogenide sources,[71,72] it is generally accepted that cadmium and chalcogen sources form a complex in the initial stage of the reaction. Subsequently, this complex encounters an oxygen donor that polarizes the phosphorus–chalcogen bond leading to its rupture. This results in a cadmium–chalcogen bond and the corresponding phosphine oxide (here, **TCEP**=O). The proposed mechanism is illustrated in Fig. 10a.

To validate this hypothesis, a **CdTe** synthesis was carried out in ^{18}O-labelled water. After the reaction, the **CdTe** QDs were separated by sedimentation and the supernatant was analyzed by LC-MS (Fig. 10b and see Section S5.13 of the ESI†). The mass spectra are compared with a reference peak of **TCEP**=^{16}O. A +2 shift in the molecular ion was visible between the reference **TCEP**=^{16}O and the **TCEP**=^{18}O produced during our experiment. Thus, in an aqueous environment, water acts as the oxygen donor, while in an organic environment, acetate is commonly seen as the oxygen donor.[71,72] This conclusion also explains the decrease of pH that was noticed during our optimization under aqueous conditions.

Further optimization was performed to maximize the QD metrics, such as the photoluminescence quantum yield (PLQY) and the FWHM (see Section S4.9 of the ESI†). To this end, the following parameter boundaries were defined as follows: temperatures from 130 °C to 200 °C; residence time from 45 s to 60 s, and a Cd/Te ratio from 5 to 7.5. The results of this screening are presented in Fig. 11. The general trend observed is the formation of larger particles under higher temperature and longer residence time. While particle growth comes with an increased PLQY, it also broadens the size distribution (larger FWHM). At a given temperature, a longer residence time gives larger particles with an improved PLQY.

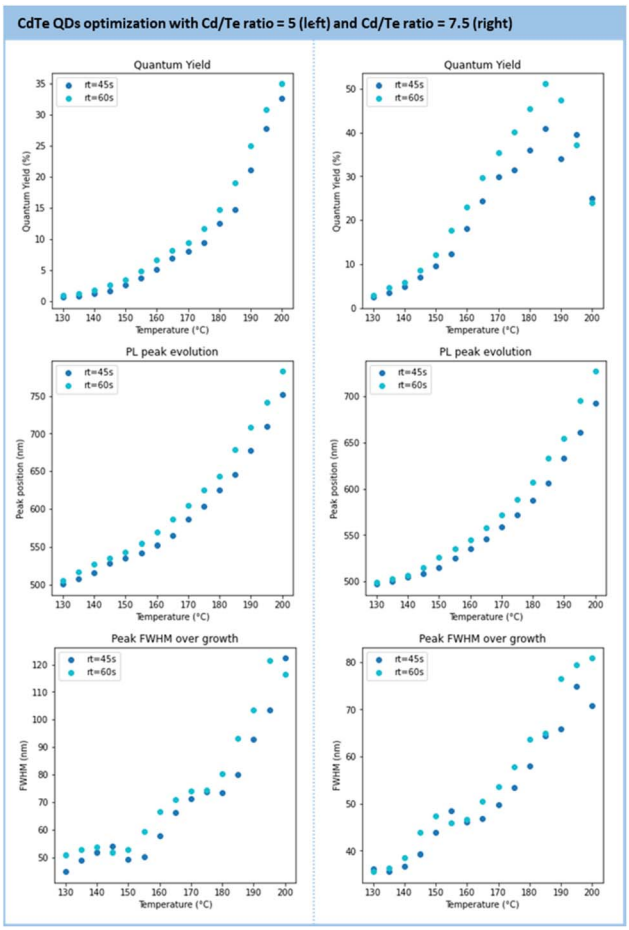

Fig. 11 Results of the main metrics to characterize the **CdTe** QDs (PLQY, PL peak position, FWHM) under various temperatures and residence times for a Cd/Te ratio of 5 (left) and 7.5 (right).

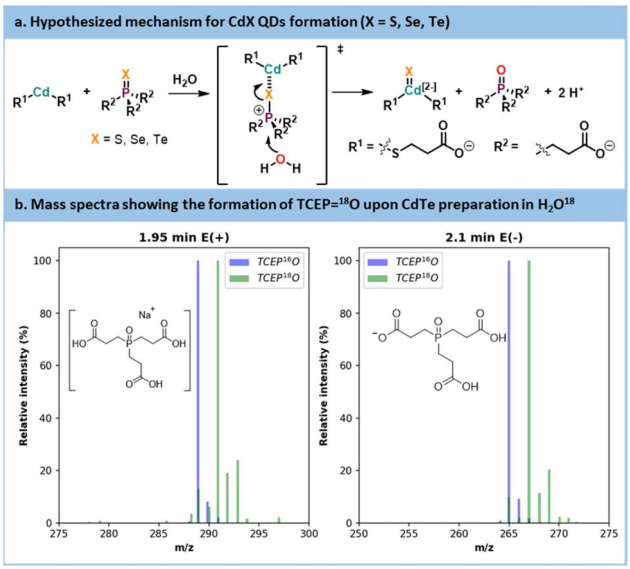

Fig. 10 (a) Hypothesized mechanism for **CdX** QDs formation. (b) Mass spectra of **TCEP**=^{18}O obtained from synthesis using labelled $H_2{}^{18}O$ and a reference of **TCEP**=^{16}O.

The series conducted with 5 and 7.5 equivalents of **Cd(3-MPA)$_2$** gave the most impactful observations. Firstly, the PLQY is higher with 7.5 equivalents (>50%) than with 5 equivalents (32%) and the emission maximum is blue-shifted from 790 nm (5 eq equiv.) to 640 nm (7.5 equiv.). The properties achieved with these particles align with recent reports on hydrothermal **CdTe** QDs.[73–75] Secondly, a large excess of Cd precursors improves the size distribution as the FWHM is enhanced with 7.5 equivalents. However, the size range accessible with 7.5 equivalents of Cd is narrower (from 500 nm to 720 nm) compared to 5 equivalents (500 nm to 770 nm). Based on these observations, the conditions with a 7.5 Cd/Te ratio were selected for scalability trials.

Scalability trials for CdTe QDs synthesis

The pilot scale setup is depicted in Fig. 12a and b (for more details, see Section S4.10 of the ESI†). It consists of 2 concatenated reactors: an upstream generator of **TCEP**=Te, (see Fig. 7), and a downstream mesofluidic reactor for the formation of the

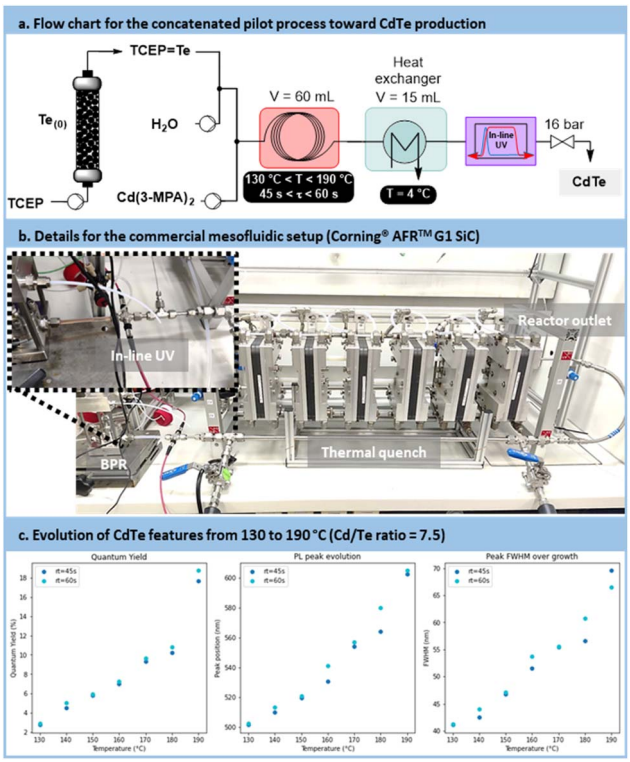

Fig. 12 (a) Simplified flow chart of the mesofluidic setup used for the scalability trials toward **CdTe** (b) photograph of the experimental setup, featuring a Corning® Advanced-Flow Reactor™ G1 SiC (60 mL of internal volume). (c) Comparison of the **CdTe** QDs main characteristics (prepared at temperatures ranging from 130 °C to 190 °C and residence times of 45 s or 60 s).

CdTe. The latter mesofluidic reactor is a commercial pilot scale unit (Corning® Advanced-Flow™ G1 SiC Reactor, equipped with 6 Silicon Carbide fluidic modules connected in series and a 60 mL total internal volume). Postreaction operations include a tube-in-tube heat exchanger, an in-line UV/Vis flow cell with a 5 mm optical pathway and a back pressure regulator prior to sample collection.

Samples were prepared at temperatures ranging from 130 °C to 190 °C, with residence times of 45 s or 60 s. The results indicated, similar to the lab-scale trials, that higher process temperatures and longer residence times resulted in larger particles (Fig. 12c). This was evidenced by a red shift in absorbance and emission peaks, along with an increased PLQY. However, this was counterbalanced by a broader size distribution, resulting in an increase in the FWHM.

The comparison between the results obtained with the microfluidic and mesofluidic setups highlights disparities. Metrics achieved by the mesofluidic reactor were lower than those observed in the microfluidic setup. Specifically, the emission range was narrower, spanning from 500 nm to 600 nm compared to 500 nm to 650 nm. The PLQY was also reduced, reaching approximately 18%, *vs.* 40% at an emission of 600 nm under microfluidic conditions. Additionally, size distribution metrics were less favorable in the mesofluidic setup, with a FWHM ranging from 40 nm to 70 nm compared to 35 nm to 60 nm. This disparity was attributed to the much higher turbulence within the mesofluidic reactor. High turbulences are likely to accelerate the recombination of nuclei, resulting in higher QD concentrations but with smaller particles under similar reaction conditions. Nevertheless, this scale-up demonstrates the relevance of the concatenated approach, enabling the production of **CdTe** QDs at a rate of 80 mL min^{-1}. As it is, the mesofluidic process allows the preparation of up to 40 g day^{-1} of **CdTe** QDs with a relative quantum yield of 18%.

Conclusions

This study introduces a novel water-soluble chalcogen vehicle that can be successfully transferred to a cadmium source, resulting in the formation of **CdX** (X = S, Se, Te) QDs in water. The preparation of **TCEP**=X (X = S, Se, Te) was optimized, with a focus on the influence of factors such as pH, chalcogen excess, mixing efficiency, and reagent granulometry, using a DoE approach. Following this optimization, *in situ* monitoring of the reaction was carried out at various temperatures using *in situ* Raman spectroscopy. The kinetic data generated allowed for real-time observation of the formation of **TCEP**=X species and the identification of the reaction mechanism, which occurs at the surface of the chalcogen particles. Over time, the reaction rate decreased due to surface degradation. Based on these observations, the process was successfully transposed in flow conditions using a packed-bed approach. Columns were filled with elemental chalcogens (S, Se, Te) and were operated in parallel for the on-demand production of the desired **TCEP**=X (X = S, Se, Te) precursors from the same feed of **TCEP**. Such an innovative approach achieved impressive productivity levels and was eventually amenable to pilot-scale production.

Following the successful transposition of precursor generation into a microfluidic, this step was concatenated with the preparation of **CdX** (X = S, Se, Te) QDs. The resulting nanoparticles were characterized using HRTEM and P-XRD, revealing nanosized spherical shapes with a cubic crystal lattice structure. Surface analysis (XPS) shows that the particles are mostly surrounded by 3-mercaptopropionic acid (thiolate and acetate groups). An alloy of $\mathbf{CdX}_n\mathbf{S}_{n-1}$ (X = Se, Te) is formed on the surface of their respective QDs.

The entire process was transposed to pilot scale in a mesofluidic reactor and demonstrated for the production of **CdTe** QDs. The pilot scale setup produced up to 80 mL min^{-1} of stable (>5 months) **CdTe** QDs. A daily production of up to 40 g per day of **CdTe** QDs exhibiting an 18% PLQY was achieved (51% PLQY at the microfluidic scale). Moreover, biocompatible **CdSe**/**ZnS** core–shell QDs were prepared with a concatenated approach. Such unprecedented processes under scalable flow conditions open new avenues for accessing aqueous QDs.

Data availability

The data supporting this article have been included as part of the ESI.†

Author contributions

GP designed and performed the experiments, analyzed the results, and wrote the first draft of the manuscript and the ESI.† CM designed the Raman in-line batch experiments, provided technical assistance for the data treatment and the kinetic model and proofread the manuscript. PB designed and performed a preliminary study on the preparation of **TCEP**═Se, analyzed the data and contributed to the redaction of the manuscript. JCMM designed the concepts, supervised the research, and wrote the manuscript.

Conflicts of interest

There are no conflicts to declare.

Acknowledgements

This work was supported by the Service Public de Wallonie (Win2Wal 2018 Program, QD3Drops Project). Computational resources were provided by the "Consortium des Équipements de Calcul Intensif" (CÉCI), funded by the "Fonds de la Recherche Scientifique de Belgique" (F. R. S.-FNRS) under Grant No. 2.5020.11a and by the Walloon Region. The authors also thank Marc Winter and Dr Guillaume Gauron (Corning SAS) for their technical support and the loan of the pilot-scale mesofluidic equipment. The TEM pictures were realized at the CAREM microscopy facility of the University of Liège. The authors also acknowledge Dr H. Hellwig for his help with the scalability trials, Prof. B. Leyh (ULiège) for the stimulating discussions on kinetics, Prof. B. Vertruyen (ULiège) for acquiring the PXRD data, Dr P. Compère (ULiège) for the HRTEM data, Prof. S. Hermans and P. Eloy for the XPS data.

Notes and references

1 A. I. Ekimov and A. A. Onushchenko, *JETP Lett.*, 1981, **34**, 363–366.
2 R. Rossetti, S. Nakahara and L. E. Brus, *J. Chem. Phys.*, 1983, **79**, 1086–1088.
3 L. Brus, *J. Chem. Phys.*, 1984, **80**, 4403–4409.
4 C. B. Murray, D. J. Norris and M. G. Bawendi, *J. Am. Chem. Soc.*, 1993, **115**, 8706–8715.
5 L. Brus, *J. Phys. Chem.*, 1986, **90**, 2555–2560.
6 S. Liu, M. Li, K. Xiong, J. Gao, X. Lan, D. Zhang, L. Gao, J. Zhang and J. Tang, *Nano Res.*, 2023, **16**, 2392–2398.
7 L. Hu, Q. Zhao, S. Huang, J. Zheng, X. Guan, R. Patterson, J. Kim, L. Shi, C. H. Lin, Q. Lei, D. Chu, W. Tao, S. Cheong, R. D. Tilley, A. W. Y. Ho-Baillie, J. M. Luther, J. Yuan and T. Wu, *Nat. Commun.*, 2021, **12**, 1–9.
8 L. Suhyeon, H. Donghyo, Y. Suk-Young, Y. Heesun, B. Wan Ki and K. Jeonghun, *Nano Res.*, 2022, **15**, 6477–6482.
9 W. Cao, C. Xiang, Y. Yang, Q. Chen, L. Chen, X. Yan and L. Qian, *Nat. Commun.*, 2018, **9**, 2–7.
10 S. Park, B. J. Kim, T. Y. Kim, E. Y. Jung, K. M. Lee, J. A. Hong, W. Jeon, Y. Park and S. J. Kang, *J. Mater. Chem. C*, 2021, **9**, 2550–2560.
11 J. Leemans, V. Pejović, E. Georgitzikis, M. Minjauw, A. B. Siddik, Y. H. Deng, Y. Kuang, G. Roelkens, C. Detavernier, I. Lieberman, P. E. Malinowski, D. Cheyns and Z. Hens, *Adv. Sci.*, 2022, **9**, 1–8.
12 X. Wu, S. Xie, C. Liu, C. Zhou, J. Lin, J. Kang, Q. Zhang, Z. Wang and Y. Wang, *ACS Catal.*, 2019, **9**, 8443–8451.
13 C. Campalani, G. Petit, J. C. M. Monbaliu, M. Selva and A. Perosa, *ChemPhotoChem*, 2023, **7**, 1–8.
14 A. Kumari, A. Sharma, U. Malairaman and R. R. Singh, *J. Lumin.*, 2018, **199**, 174–182.
15 D. Bera, L. Qian, T. K. Tseng and P. H. Holloway, *Materials*, 2010, **3**, 2260–2345.
16 L. J. Pan, J. W. Tu, H. T. Ma, Y. J. Yang, Z. Q. Tian, D. W. Pang and Z. L. Zhang, *Lab Chip*, 2018, **18**, 41–56.
17 M. Guidi, P. H. Seeberger and K. Gilmore, *Chem. Soc. Rev.*, 2020, **49**, 8910–8932.
18 L. Capaldo, Z. Wen and T. Noël, *Chem. Sci.*, 2023, 4230–4247.
19 J. B. Edel, R. Fortt, J. C. DeMello and A. J. DeMello, *Chem. Commun.*, 2002, **2**, 1136–1137.
20 E. M. Chan, R. A. Mathies and A. P. Alivisatos, *Nano Lett.*, 2003, **3**, 199–201.
21 B. K. H. Yen, N. E. Stott, K. F. Jensen and M. G. Bawendi, *Adv. Mater.*, 2003, **15**, 1858–1862.
22 S. Marre, J. Park, J. Rempel, J. Guan, M. G. Bawendi and K. F. Jensen, *Adv. Mater.*, 2008, **20**, 4830–4834.
23 Y. Pu, F. Cai, D. Wang, J. X. Wang and J. F. Chen, *Ind. Eng. Chem. Res.*, 2018, **57**, 1790–1802.
24 M. S. Naughton, V. Kumar, Y. Bonita, K. Deshpande and P. J. A. Kenis, *Nanoscale*, 2015, **7**, 15895–15903.
25 M. Abolhasani, C. W. Coley, L. Xie, O. Chen, M. G. Bawendi and K. F. Jensen, *Chem. Mater.*, 2015, **27**, 6131–6138.
26 A. Toyota, H. Nakamura, H. Ozono, K. Yamashita, M. Uehara and H. Maeda, *J. Phys. Chem. C*, 2010, **114**, 7527–7534.
27 H. Nakamura, A. Tashiro, Y. Yamaguchi, M. Miyazaki, T. Watari, H. Shimizu and H. Maeda, *Lab Chip*, 2004, **4**, 237–240.
28 R. Kikkeri, P. Laurino, A. Odedra and P. H. Seeberger, *Angew. Chem., Int. Ed.*, 2010, **49**, 2054–2057.
29 M. Kawa, H. Morii, A. Ioku, S. Saita and K. Okuyama, *J. Nanopart. Res.*, 2003, **5**, 81–85.
30 W. Wang, Y. Guo, C. Tiede, S. Chen, M. Kopytynski, Y. Kong, A. Kulak, D. Tomlinson, R. Chen, M. McPherson and D. Zhou, *ACS Appl. Mater. Interfaces*, 2017, **9**, 15232–15244.
31 Y. Shen, M. Abolhasani, Y. Chen, L. Xie, L. Yang, C. W. Coley, M. G. Bawendi and K. F. Jensen, *Angew. Chem., Int. Ed.*, 2017, **56**, 16333–16337.
32 A. M. Nightingale and J. C. De Mello, *J. Mater. Chem.*, 2010, **20**, 8454–8463.
33 A. R. M. De Oliveira, L. Piovan, F. Simonelli, A. Barison, M. D. F. C. Santos and M. B. M. De Mello, *J. Organomet. Chem.*, 2016, **806**, 54–59.
34 I. Shestopalov, J. D. Tice and R. F. Ismagilov, *Lab Chip*, 2004, **4**, 316–321.
35 J. Dai, X. Yang, M. Hamon and L. Kong, *Chem. Eng. J.*, 2015, **280**, 385–390.
36 X. Yang, Q. Wang, Y. Tao and H. Xu, *J. Chem. Res.*, 2002, 160–161.

37 G. Emonds-alt, M. Lismont, G. Eppe and J. M. Monbaliu, *J. Chem. Educ.*, 2017, **94**, 775–780.
38 R. C. Mbwahnche, L. B. Matyushkin, O. A. Ryzhov, O. A. Aleksandrova and V. A. Moshnikov, *J. Phys.: Conf. Ser.*, 2016, **741**, 1–6.
39 D. Das and R. K. Dutta, *J. Photochem. Photobiol., A*, 2020, **400**, 112709.
40 S. Kubendhiran, Z. Bao, K. Dave and R. S. Liu, *ACS Appl. Nano Mater.*, 2019, **2**, 1773–1790.
41 P. Bianchi, A. Dubart, M. Moors, D. Cornut, G. Duhirwe, J. Ampurdanés Vilanova and J. C. M. Monbaliu, *React. Chem. Eng.*, 2023, **8**, 1565–1575.
42 J. C. M. Monbaliu and J. Legros, *Lab Chip*, 2022, **23**, 1349–1357.
43 R. Morodo, R. Riva, N. M. S. van den Akker, D. G. M. Molin, C. Jérôme and J. C. M. Monbaliu, *Chem. Sci.*, 2022, **13**, 10699–10706.
44 D. V. Silva-Brenes, N. Emmanuel, V. López Mejías, J. Duconge, C. Vlaar, T. Stelzer and J. C. M. Monbaliu, *Green Chem.*, 2022, **24**, 2094–2103.
45 Y. Chen, S. Renson and J. C. M. Monbaliu, *Angew. Chem., Int. Ed.*, 2022, **61**, e202210146.
46 P. Bianchi, G. Petit and J. C. M. Monbaliu, *React. Chem. Eng.*, 2020, **5**, 1224–1236.
47 J. A. Burns, J. C. Butler, J. Moran and G. M. Whitesides, *J. Org. Chem.*, 1991, **56**, 2648–2650.
48 N. Ollivier, T. Toupy, R. C. Hartkoorn, R. Desmet, J. C. M. Monbaliu and O. Melnyk, *Nat. Commun.*, 2018, **9**, 1–12.
49 V. Agouridas, O. El Mahdi, V. Diemer, M. Cargoët, J. C. M. Monbaliu and O. Melnyk, *Chem. Rev.*, 2019, **119**, 7328–7443.
50 D. J. Cline, S. E. Redding, S. G. Brohawn, J. N. Psathas, J. P. Schneider and C. Thorpe, *Biochemistry*, 2004, **43**, 15195–15203.
51 P. Kumar, T. Chiku, M. J. Carvan and D. S. Sem, *Anal. Biochem.*, 2006, **352**, 265–273.
52 C. R. Schlieve, A. Tam, B. L. Nilsson, C. J. Lieven, R. T. Raines and L. A. Levin, *Exp. Eye Res.*, 2006, **83**, 1252–1259.
53 J. Ge, L. Zhou, F. Zhao and H. Dong, *J. Org. Chem.*, 2017, **82**, 12613–12623.
54 S. Dery, P. S. Reddy, L. Dery, R. Mousa, R. N. Dardashti and N. Metanis, *Chem. Sci.*, 2015, **6**, 6207–6212.
55 N. Ollivier, A. Blanpain, E. Boll, L. Raibaut and O. Melnyk, *Org. Lett.*, 2014, **16**, 4032–4035.
56 G. Tallec, C. Loh, B. Liberelle, A. Garcia-Ac, S. V. Duy, S. Sauvé, X. Banquy, F. Murschel and G. De Crescenzo, *Bioconjugate Chem.*, 2018, **29**, 3866–3876.
57 A. Faucher and C. Grand-maître, *Synth. Commun.*, 2003, **33**, 3503–3511.
58 A. Krezel, R. Latajka, G. D. Bujacz and W. Bal, *Inorg. Chem.*, 2003, **42**, 1994–2003.
59 J. Podlaha and J. Podlahová, *Collect. Czech. Chem. Commun.*, 1973, **38**, 1730–1736.
60 Y. Iida, T. Yamaguchi, T. Tanaka and S. Nakayama, *J. Nucl. Sci. Technol.*, 2010, **47**, 431–438.
61 S. R. Alvarado, I. A. Shortt, H. J. Fan and J. Vela, *Organometallics*, 2015, **34**, 4023–4031.
62 M. A. Vairavamurthy, W. S. Goldenberg, S. Ouyang and S. Khalid, *Mar. Chem.*, 2000, **70**, 181–189.
63 C. A. M. Bonilla, M. H. T. Flórez, D. R. Molina Velasco and V. V. Kouznetsov, *New J. Chem.*, 2019, **43**, 8452–8458.
64 B. Zeng, G. Palui, C. Zhang, N. Zhan, W. Wang, X. Ji, B. Chen and H. Mattoussi, *Chem. Mater.*, 2018, **30**, 225–238.
65 C. Giansante and I. Infante, *J. Phys. Chem. Lett.*, 2017, **8**, 5209–5215.
66 H. Li, W. Y. Shih and W. H. Shih, *Ind. Eng. Chem. Res.*, 2007, **46**, 2013–2019.
67 Q. Wang, Y. Xu, X. Zhao, Y. Chang, Y. Liu, L. Jiang, J. Sharma, D. K. Seo and H. Yan, *J. Am. Chem. Soc.*, 2007, **129**, 6380–6381.
68 G. Ramalingam, K. V. Saravanan, T. K. Vizhi, M. Rajkumar and K. Baskar, *RSC Adv.*, 2018, **8**, 8516–8527.
69 D. Mo, L. Hu, G. Zeng, G. Chen, J. Wan, Z. Yu, Z. Huang, K. He, C. Zhang and M. Cheng, *Appl. Microbiol. Biotechnol.*, 2017, **101**, 2713–2733.
70 P. Bianchi and J.-C. M. Monbaliu, *Angew. Chem., Int. Ed.*, 2024, **63**, e202311526.
71 H. Liu, J. S. Owen and A. P. Alivisatos, *J. Am. Chem. Soc.*, 2007, **129**, 305–312.
72 R. García-Rodríguez and H. Liu, *J. Am. Chem. Soc.*, 2012, **134**, 1400–1403.
73 T. Jiawei, L. Yan, W. Jiexin, C. Jianfeng, S. Baochang and S. Lei, *New J. Chem.*, 2015, **39**, 4488–4493.
74 E. Ying, D. Li, S. Guo, S. Dong and J. Wang, *PLoS One*, 2008, **3**, 1–7.
75 C. S. M. Martins, A. L. Silva, L. P. de Gouveia, I. Çaha, O. Bondarchuk, A. P. LaGrow, F. L. Deepak and J. A. V. Prior, *Chemosensors*, 2024, **12**, 12040070.